Space Weather®

RESEARCH ARTICLE
10.1029/2022SW003085

Special Section:
NOAA's Space Weather Missions and Instruments

Validation of the DSCOVR Spacecraft Mission Space Weather Solar Wind Products

Paul T. M. Loto'aniu[1,2], K. Romich[1,2], W. Rowland[2], S. Codrescu[1,2], D. Biesecker[3,4], J. Johnson[1,5], H. J. Singer[5], A. Szabo[4], and M. Stevens[6]

[1]Cooperative Institute for Research in Environmental Sciences, University of Colorado Boulder, Boulder, CO, USA, [2]National Centers for Environmental Information, National Oceanic and Atmospheric Administration, Boulder, CO, USA, [3]National Environmental Satellite, Data, and Information Service, National Oceanic and Atmospheric Administration, Silver Spring, MD, USA, [4]Goddard Space Flight Center, National Aeronautics and Space Administration, Greenbelt, MD, USA, [5]Space Weather Prediction Center, National Oceanic and Atmospheric Administration, Boulder, CO, USA, [6]Center for Astrophysics, Harvard and Smithsonian, Cambridge, MA, USA

Abstract In this paper, we present a statistical validation of the Deep Space Climate Observatory (DSCOVR) solar wind data in the operational space weather archive. The DSCOVR observations of the interplanetary magnetic field (IMF), solar wind velocity, density, and temperature were hourly averaged and compared to measurements from NASA's Advanced Composition Explorer (ACE) and *Wind* spacecraft. Hourly averages, in general, show good correlations between the satellites for the IMF, solar wind velocity Geocentric Solar Ecliptic (GSE) v_x-component, and density. During the period covered by this study (spanning from late July 2016, when DSCOVR went operational, to the end of 2020), the DSCOVR products show no clear evidence of permanent degradation. However, for plasma parameters, there were periods of disagreement with ACE and *Wind*. The correlation coefficients (Pearson's *r*) calculated over the entire study period were similar or the same between DSCOVR versus *Wind* and DSCOVR versus ACE. For comparisons between DSCOVR and *Wind*, the IMF B_x and B_y GSE *r* were 0.94 and 0.96, respectively, while *r* for the IMF GSE B_z-component was 0.88. For solar wind velocity, *r* was found to be 0.96 for the GSE v_x-component, compared with 0.30 for v_y and 0.33 for v_z. For density, *r* was found to be 0.84. DSCOVR density observations tend to overestimate compared to *Wind* values when the solar wind densities are low (below ~5/cc), while the agreement between the two spacecraft on IMF measurements tends to increase with decreasing spatial separation.

Plain Language Summary We present a statistical validation of space weather operational products derived from measurements onboard a National Oceanic and Atmospheric Administration (NOAA) spacecraft orbiting at about 1.5 million kilometers toward the Sun from Earth. Spacecraft observations of the solar wind magnetic field, velocity, density, and temperature were hourly averaged and compared to measurements from two other spacecraft in similar orbits. Hourly averages, in general, show good correlations between the spacecraft for solar wind magnetic field, the main component of velocity and density. However, for solar wind plasma parameters, there were periods of disagreement with the other two spacecraft. The NOAA spacecraft density observations tend to overestimate when compared to one of the other spacecraft measurements when the solar wind densities are low, while the agreement between these two spacecraft on magnetic field measurements tends to increase with decreasing spacecraft separation.

Key Points:

- We validate the Deep Space Climate Observatory operational space weather data products
- Magnetic field data showed good statistical agreement with *Wind* and Advanced Composition Explorer (ACE) data
- Solar wind velocity Geocentric Solar Ecliptic v_x-component and density also showed good statistical agreement with *Wind* and ACE data

Correspondence to:
P. T. M. Loto'aniu,
paul.lotoaniu@noaa.gov

Citation:
Loto'aniu, P. T. M., Romich, K., Rowland, W., Codrescu, S., Biesecker, D., Johnson, J., et al. (2022). Validation of the DSCOVR spacecraft mission space weather solar wind products. *Space Weather*, *20*, e2022SW003085. https://doi.org/10.1029/2022SW003085

Received 5 MAR 2022
Accepted 12 SEP 2022

1. Introduction

The National Oceanic and Atmospheric Administration (NOAA) Deep Space Climate Observatory (DSCOVR) mission was launched in February 2015 to the 1st Lagrange point (L1), which is located about 1.5 million kilometers from Earth, toward the sun, along the Sun-Earth line. The DSCOVR mission is a NOAA space weather operational mission that provides and sustains the United States' real-time solar wind monitoring capabilities, which are critical to the accuracy and lead time of NOAA's space weather alerts and forecasts. NOAA funded NASA to refurbish the DSCOVR spacecraft and solar wind instruments, develop the command and control portion of the ground segment, and manage the launch and activation of the satellite. The United States Air Force funded and managed the SpaceX Falcon 9 launch services for DSCOVR. On 7 June 2015, DSCOVR reached its final L1 destination, and in late October 2015, after checkout and post-launch testing, NOAA officially took command of the DSCOVR satellite. DSCOVR became the NOAA operational L1 solar wind monitor on 27 July 2016 at

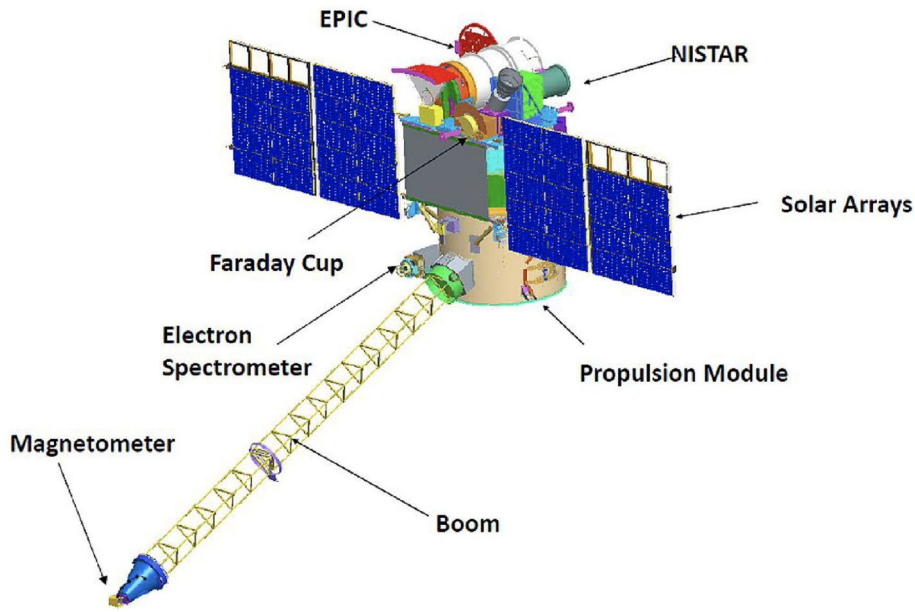

Figure 1. Diagram of the Deep Space Climate Observatory spacecraft with instruments indicated (Szabo, 2014).

16:00 UTC when it began providing data for space weather forecasting at the NOAA Space Weather Prediction Center (SWPC).

The main science payloads onboard DSCOVR are the PlasMag suite, which includes the solar wind monitoring plasma (Faraday Cup) and magnetometer instruments, the Earth-observing NIST Advanced Radiometer (NISTAR), and the Earth Polychromatic Imaging Camera (EPIC). Figure 1 shows the spacecraft with instrument payloads indicated. Of interest in this study is the PlasMag suite, which measures the solar wind particles and the interplanetary magnetic field (B_{IMF}) for NOAA space weather predictions. There is also an electrostatic analyzer (ESA) spectrometer on DSCOVR, which is not a requirement by NOAA for space weather operations.

NOAA operates DSCOVR from its NOAA Satellite Operations Facility (NSOF) in Suitland, Maryland, and distributes the data to its users and partner agencies. NOAA processes the space weather data, providing products and forecasts through the NOAA-SWPC in Boulder, Colorado, and archives the data at the NOAA National Centers for Environmental Information (NCEI), also in Boulder, Colorado. NASA is responsible for processing the EPIC data.

The focus of this study is the validation of the NOAA-NCEI DSCOVR space weather or PlasMag instrument suite archive. The validation effort is restricted to the 1-min or lower resolution data products and covers the years 2016–2020. Validate against data from NASA's Advanced Composition Explorer (ACE) and *Wind* spacecraft missions, which were both located at L1 during the validation interval.

When interpreting the results presented, it should be kept in mind that the NOAA-NCEI DSCOVR archive contains data collected during real-time NOAA operations, whereas the ACE and *Wind* data sets may have undergone further post-processing to improve science quality. Hence, we expect to observe more issues, such as missing data in the DSCOVR archive. This is further emphasized by the fact that the DSCOVR spacecraft has experienced multiple issues since commissioning that affect both the quality and availability of the space weather data.

In the following paper, Section 2 describes the DSCOVR PlasMag instruments. Section 3 discusses the methodology for the validation and data availability, while Section 4 shows the results. Finally, conclusions are discussed in Section 5.

2. The DSCOVR Space Weather Instruments

2.1. The Magnetometer

The DSCOVR triaxial fluxgate magnetometer (MAG), which measures the interplanetary vector magnetic field (B_{IMF}) and is shown on the left in Figure 2, is located at the tip of a 4.0 m boom to minimize the effect of spacecraft

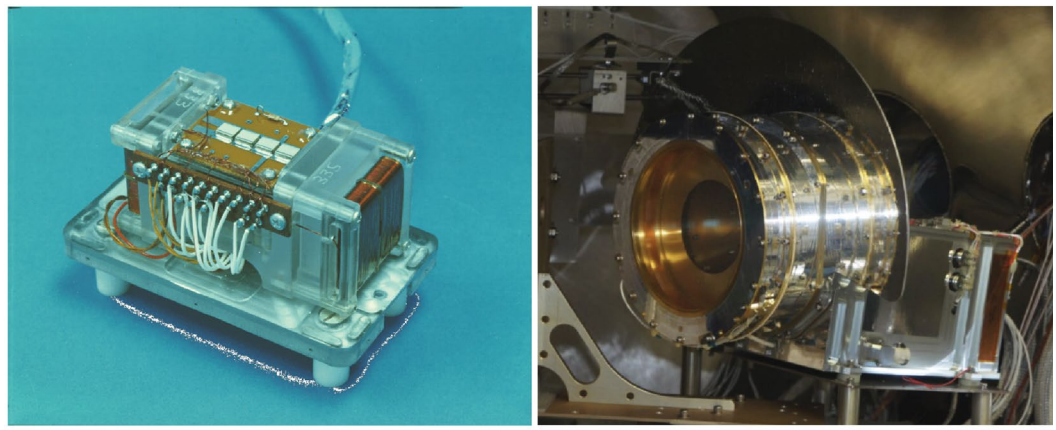

Figure 2. Left: A photo of the Deep Space Climate Observatory (DSCOVR) magnetometer instrument (Szabo, 2015). Right: a photo of the DSCOVR Faraday Cup instrument (Kasper et al., 2013).

fields. The MAG was provided by the NASA Goddard Space Flight Center (GSFC) in Greenbelt, Maryland, and underwent prelaunch instrument- and spacecraft-level tests also at NASA-GSFC (Connerney, 2013). These tests establish instrument prelaunch calibration parameters, such as zero offsets, gains or scale factors, alignment, noise, and spacecraft magnetic signature at the sensor location.

Table 1 shows the requirements and ground performance of the MAG (Szabo & Koval, 2016). Currently, the NOAA-SWPC operational requirement is for the B_{IMF} product at 1-min cadence. However, the MAG instrument on DSCOVR samples at 50 samples/sec. The instrument has multiple ranges with the highest reaching 65,500 nT for ground calibration.

On orbit, the DSCOVR spacecraft underwent a series of rolls in order to estimate MAG zero offsets. Independently, offsets were also determined using solar wind Alfvenic wave rotation methods (Belcher, 1973; Belcher et al., 1969; Davis & Smith, 1968) to ensure consistent offset values (Szabo, 2015). In operations, the spacecraft continues to undergo maneuvers about every 6 weeks to redetermine offsets, and the Alfvenic method is also used to verify results and determine the roll axis offset. The calibration analysis is performed by NASA-GSFC and updated offsets are sent to SWPC for operational use.

The space weather products created from the MAG observations are the total magnetic field, the vector magnetic field in Geocentric Solar Ecliptic (GSE) and GSM coordinates, and the IMF clock and polar angles, θ and ϕ, both in GSE and GSM coordinates. The NOAA archive MAG products are daily files at a full resolution (50 Hz), 1-s cadence, and 1-min cadence. However, since the operational product is the 1-min data, here, we use the archived 1-min vector magnetic field data.

2.2. The Faraday Cup

The DSCOVR Faraday Cup (FC) is a retarding potential particle detector that provides high time resolution solar wind proton bulk properties (wind speed, density, and temperature) (Szabo, 2015). The FC measures the flux of positively charged solar wind particles as a function of their kinetic energy per charge. The instrument, which is shown on the right in Figure 2, consists primarily of a circular collector plate, divided into three independent 120°

Table 1
The Magnetometer Observational Requirements

Parameter	Requirements	Ground performance
B_{IMF}	3-axis vector observation in situ	N/A
Accuracy	1.0 nT/axis	0.2 nT/axis
Sample rate	1 vector/min/axis	50 vectors/sec/axis
Range	±0.1–100 nT	±0.004 (resolution) −65,500 nT

Table 2
Observational Requirements of the Deep Space Climate Observatory Faraday Cup

Parameter	Requirements	Ground performance
Velocity range	200–1,250 km/s	168–1,340 km/s
Velocity accuracy	20%	2%
Density range	1–100 cm^{-3}	0.22–219 cm^{-3}
Density accuracy	20%	20%
Temperature range	4×10^4–2×10^6 K	3.9×10^4–7.3×10^6 K
Temperature accuracy	20%	<9%
Cadence	60 s	0.25 s

sectors, positioned behind a high-voltage grid (Stevens et al., 2014). Apart from the segmentation of the collector, the DSCOVR Faraday Cup is very similar to the *Wind* Faraday Cup described by Ogilvie et al. (1995).

The FC's observational requirements and ground performance are shown in Table 2. Ground testing showed performance exceeding requirements for all parameters. However, on-orbit analysis showed that the FC data underperform during certain low solar wind conditions. This is described in Section 4.2.

3. Data and Methodology

3.1. Data Description

The solar wind parameters derived from DSCOVR data that are validated in this study against ACE and *Wind* data are those most important to current NOAA space weather operations, namely, the 1-min resolution IMF magnetic field, speed, proton density, and temperature. These parameters are archived in the DSCOVR Level 2 1-min averaged magnetometer and Faraday Cup instrument-derived netCDF data files; these files were obtained through the DSCOVR Space Weather Data Portal maintained by NOAA's National Centers for Environmental Information (NCEI) (https://www.ngdc.noaa.gov/dscovr/). A full list of the NOAA-NCEI archived DSCOVR space weather data products can be found on the portal website. The products have a code that uniquely identifies each product within the filenames; for this study, they are m1m (1-min averaged magnetometer data) and f1m (1-min Faraday Cup data). Users can also plot summaries of the DSCOVR data on the portal. It should be noted that real-time, operational, solar wind data can be obtained from NOAA's SWPC at https://www.swpc.noaa.gov/.

The ACE and *Wind* data used in this analysis were obtained from NASA's Coordinated Data Analysis Web (NASA-CDAWeb) (https://cdaweb.gsfc.nasa.gov/index.html/). In order to compare with ACE and *Wind* data over the lifetime of the DSCOVR mission, the DSCOVR data were averaged to hourly and monthly values. The NASA-CDAWeb ACE data products used were the 1-hr magnetic field (`AC_H2_MFI`) and solar wind parameters (`AC_H2_SWE`). For *Wind*, hourly averages were available for the magnetic field only (`WI_H0_MFI`), while the solar wind particle data were derived from the 92-s resolution data products (`WI_K0_SWE`).

There are higher quality products on the NASA-CDAWeb. For example, the *Wind* `WI_H1_SWE` product was produced with human in-the-loop. However, we use the K0 data because it is more similar in terms of processing steps to the real-time DSCOVR archive.

The time period considered for validation spans from 26 July 2016 (the earliest availability of NCEI DSCOVR Level 2 data) to 31 December 2020. For each satellite, we examine magnetic field strength (B_x, B_y, B_z), solar wind velocity (v_x, v_y, v_z), proton density, and proton temperature. GSE coordinates are used for both vector quantities. In the case of *Wind*, an additional step is required to find temperature values, since the parameter stored in the data repository is not temperature but most probable thermal speed (i.e., $v_{th} = \sqrt{2kT/M}$, where k is Boltzmann's constant and M is the mass of a single proton). Hence, the Kelvin temperature is given by $T = \left[M v_{th}^2/(2k)\right] \times 10^6$ with the 10^6 factor included because v_{th} is provided in km/s.

3.2. Data Availability

With the exception of the ACE Magnetic Field Investigation (MFI) data (which at time of download were unavailable on CDAWeb past 24 November 2020) and the ACE Solar Wind Electron Proton Alpha Monitor (SWEPAM) data (which at time of download were unavailable on CDAWeb past 30 June 2019), the analyses described in this paper were conducted over the full range of dates indicated above. Missing data or fill values are excluded from the study period. Additional manipulations were sometimes necessary, such as regridding to a regular timestamp that matches across data sets.

Figure 3 displays the DSCOVR B_z (GSE) magnetic field component and solar wind v_x (GSE) velocity component from 26 July 2016 to 31 December 2020 with periods of data missing from the DSCOVR MAG and FC data archives indicated by the red regions. These regions represent dates for which <75% of the available data are useable and comprise 17.2% and 17.7% of all dates considered for the MAG and FC archives, respectively.

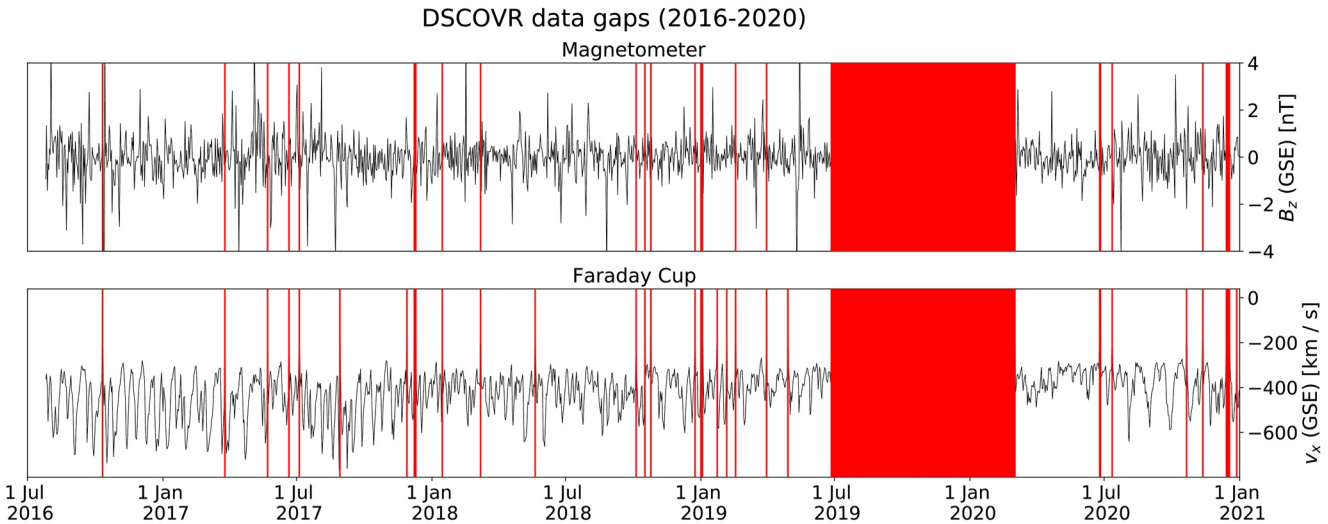

Figure 3. Visualization of Deep Space Climate Observatory (DSCOVR) magnetometer B_z component (top) and Faraday Cup solar wind v_x component (bottom) data, showing date ranges for which DSCOVR data were available for this study. The red regions represent dates for which <75% of the available data are useable.

The bulk of the DSCOVR data issues occurs in the second half of 2019 and early 2020. This was due to problems with DSCOVR's Miniature Inertial Measurement Unit (MIMU) that caused mission operations to place the spacecraft in an extended safe hold mode. The MIMU issues were not resolved until early March 2020, when DSCOVR returned to nominal operations. In addition to the MIMU issues, soon after commissioning in June 2015, DSCOVR experienced spurious reboots, which reset the spacecraft and placed it into a safe hold mode. The resets occurred infrequently and were fixed in mid-2019. Other technical issues have occurred from time-to-time that have resulted in short periods of data loss.

3.3. Statistical Methodology

We compute hourly resolution time series using DSCOVR, ACE, and *Wind* data. (Note that the year 2020 was excluded from the ACE/SWEPAM time series due to the lack of available data from NASA CDAWeb.) Using hourly averaged data, we perform linear regressions on the eight parameters of interest across each pair of satellites (DSCOVR-ACE, DSCOVR-*Wind*, and *Wind*-ACE). Since there is a measurement error in each data set, we use orthogonal-distance regression (which accounts for error in both dependent and independent variables) rather than simple ordinary-least-squares regression, which assumes a predictor variable that is free from error. Unlike ordinary-least-squares regression, which determines the equation of a linear regression line by minimizing the vertical distance from each data point to the line, orthogonal regression seeks to minimize the orthogonal distance from each data point to the line (Boggs et al., 1988). The regression analysis returns the line of best fit $y = ax + b$. We also compute the Pearson correlation coefficient r to assess the strength of the relationship, that is, the degree to which changes in one variable correspond to changes in the other.

In addition to determining correlations over the nearly 5 years of available data, we also estimate r-values for each month of data to visualize the evolution of the correlation strength for a given parameter over a multiyear period. This can provide information on instrument degradation or other instrument issues in one or both satellites. It can also be an indicator of the effects of spacecraft separation on correlation strength. We investigate variations in correlation strength in the context of (a) relative position, (b) solar wind speed, and (c) proton density. Using the hourly averages generated previously, we determine monthly averages for spacecraft separation (i.e., the physical distance between satellites in three-dimensional space) as well as the ambient solar wind parameters as measured by *Wind*. This produces a month-by-month time series of the same length as the series of parameter r-values, which can then be compared, using a second Pearson's r calculation, as an initial assessment of the degree to which fluctuations in correlation strength between spacecraft measurements correspond to fluctuations in the parameter of interest.

We also investigate whether DSCOVR over- or underestimates parameter values as compared to *Wind*, and under what physical conditions, this tends to occur. For each of the solar wind plasma parameters, as well as the

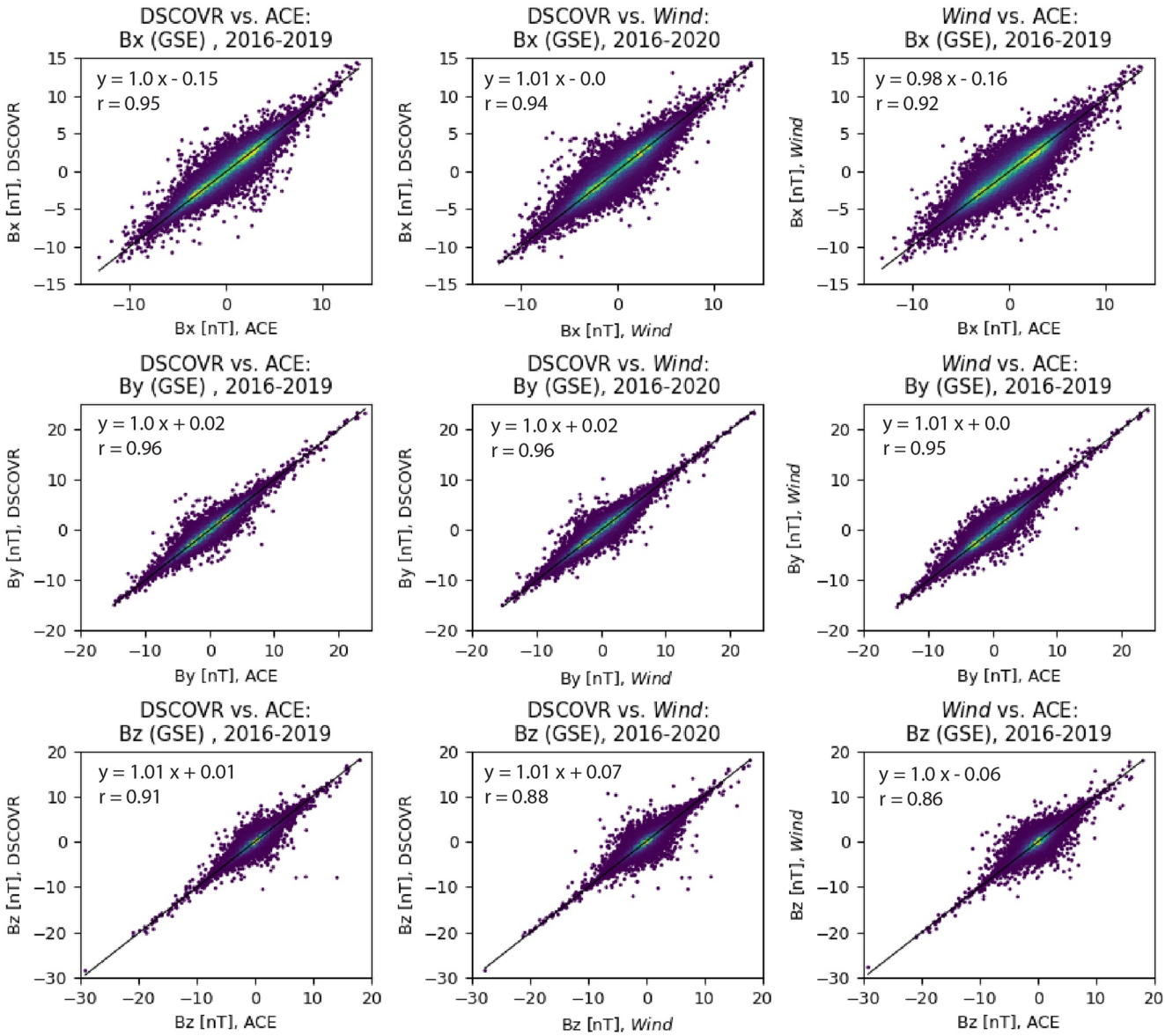

Figure 4. Scatterplots and best-fit lines for hourly average B_x (top), B_y (middle), and B_z (bottom) values across each satellite pair. Coloring of the data points indicates relative density of the data with green to yellow corresponding to higher density of data points. The Deep Space Climate Observatory (DSCOVR)-Advanced Composition Explorer (ACE) scatterplots contain 31,416 data points from 2016 to 2020; the DSCOVR-*Wind* scatterplots contain 32,129 data points from 2016 to 2020; and the *Wind*-ACE scatterplots contain 37,747 data points from 2016 to 2020. Trend line equations and correlation coefficients (Pearson's *r*) are indicated on each panel.

z-component of the IMF, we compute ratios of hourly averages as measured by DSCOVR and *Wind* (i.e., one DSCOVR/*Wind* data point for each hour from 26 July 2016 00:00 to 31 December 2020 23:00). These are sorted into bins based on solar wind speed (i.e., $|v| = \sqrt{v_x^2 + v_y^2 + v_z^2}$) and proton density, both as measured by *Wind*, and means and standard deviations are determined for each bin.

4. Validation Results

4.1. Comprehensive Regressions

Figure 4 shows scatterplots of hourly averaged magnetic field component data across different pairs of satellites over the full date range for which DSCOVR data were available (2016–2020). The colors of the data points

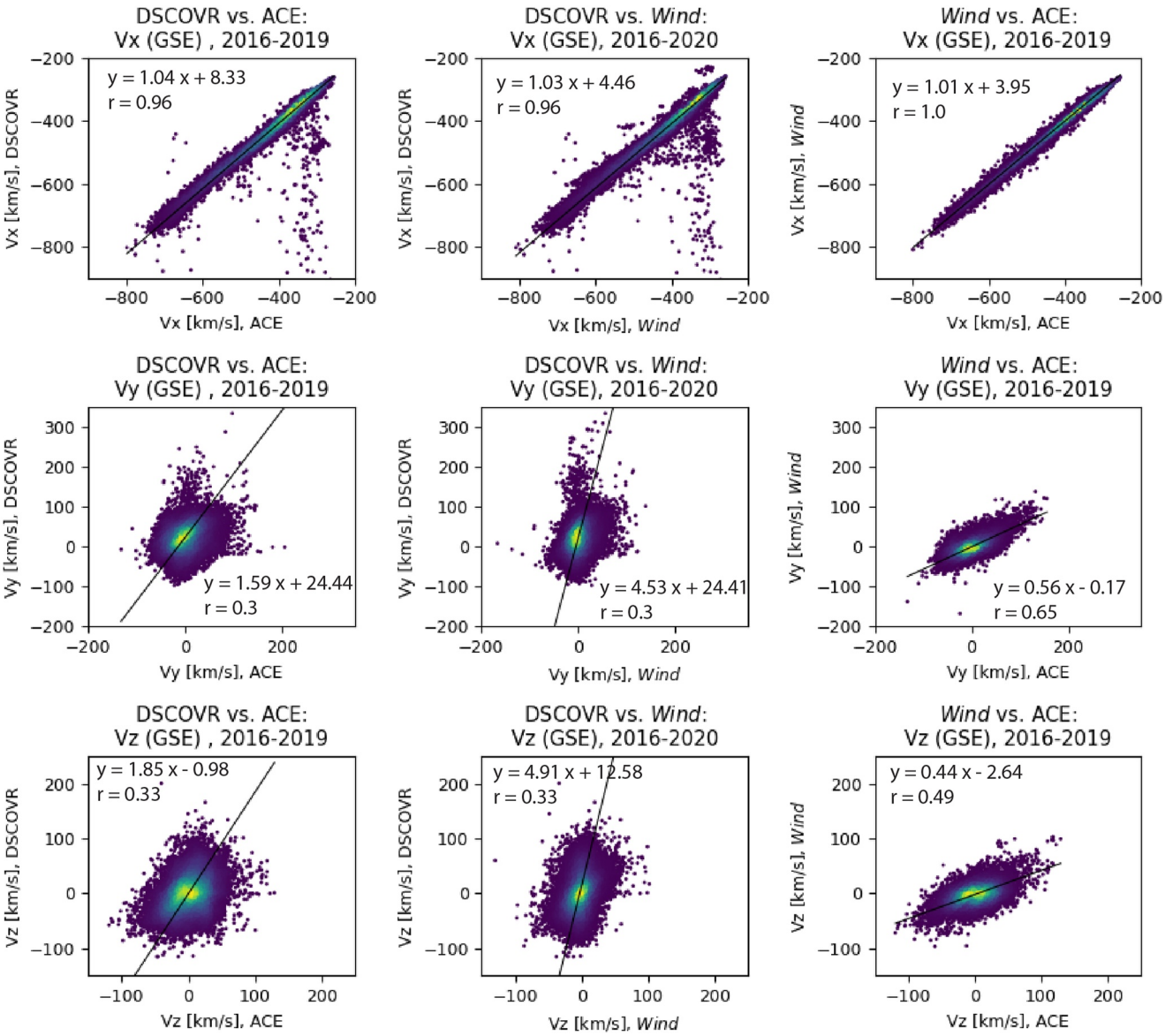

Figure 5. Scatterplots and best-fit lines for hourly average v_x (top), v_y (middle), and v_z (bottom) values across each satellite pair. Coloring of the data points indicates relative density of the data with green to yellow corresponding to higher density of data points. The Deep Space Climate Observatory (DSCOVR)-Advanced Composition Explorer (ACE) scatterplots contain 24,529 data points from 2016 to 2019; the DSCOVR-*Wind* scatterplots contain 31,430 data points from 2016 to 2020; and the *Wind*-ACE scatterplots contain 25,189 data points from 2016 to 2019. Trend line equations and correlation coefficients (Pearson's *r*) are indicated on each panel.

indicate relative density of the data in that region, where green to yellow corresponds to higher density of data points. Orthogonal-distance regression was used to estimate shown *r* values and lines of best fit. The *r* values are consistently high (above 0.8) in all cases, indicating that in general, the DSCOVR magnetometer measurements, at least hourly averaged, are in good agreement with ACE and *Wind* observations. In addition, the slope of the line-of-best fit is ∼1.0 for all comparisons, showing that there is no significant offset between DSCOVR, ACE, and *Wind* magnetic field observations.

Corresponding scatterplots and regressions for solar wind velocity components are shown in Figure 5. The agreement among the three satellites is very strong (≥0.96) for the v_x-component. As with the magnetic field components, the slope of each v_x trend line is nearly 1.0 and the *y*-intercepts are nearly zero. However, there are periods of poor agreement in the v_x-component comparisons as shown between −400 and −200 km/s in the top panels; these will be examined in Section 4.2. The *r*-values for the v_y and v_z component comparisons are lower across all

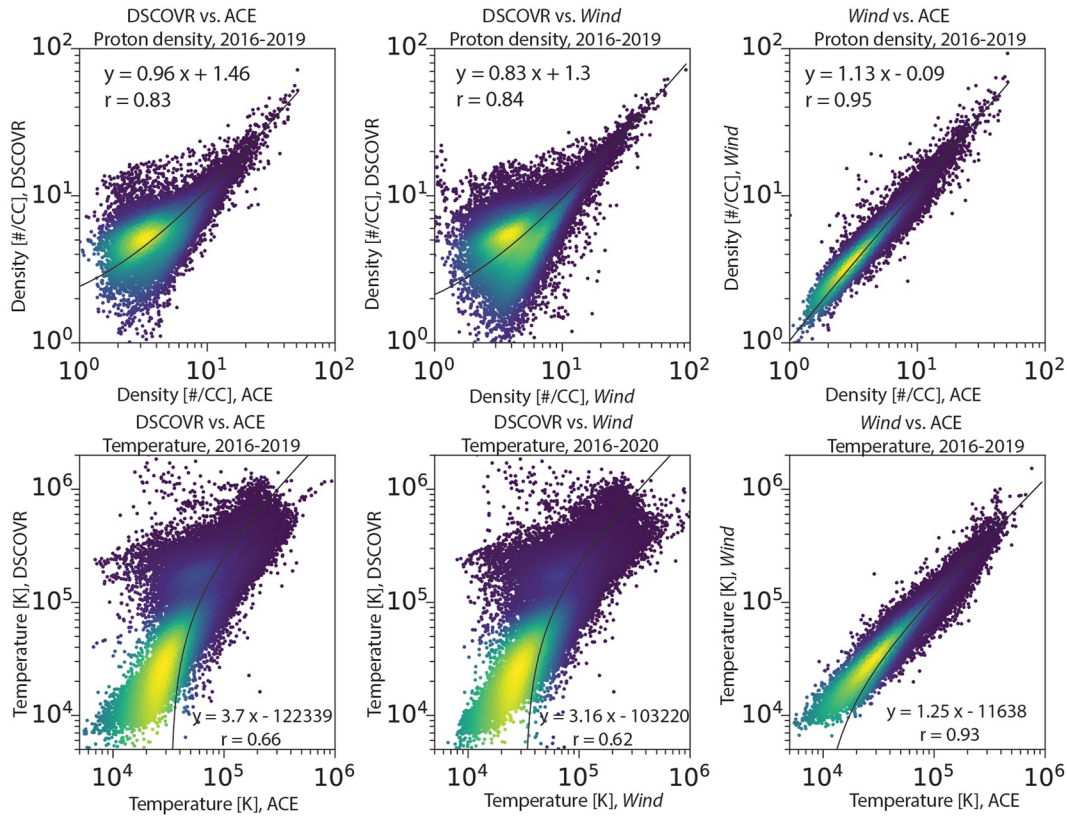

Figure 6. Upper panels: Scatterplots and best-fit lines for hourly average proton density values across each satellite pair. Lower panels: Same as upper panels but for hourly average temperature values. The coloring of the data points indicates relative density of the data with green to yellow corresponding to higher density of data points. Lines of best fit and correlation coefficients (Pearson's *r*) are also shown. For upper panels—the Deep Space Climate Observatory (DSCOVR)-Advanced Composition Explorer (ACE), DSCOVR-*Wind*, and *Wind*-ACE plots contain 13,571, 31,430, and 13,867 data points, respectively. For lower panels—The DSCOVR-ACE, DSCOVR-*Wind*, and *Wind*-ACE plots contain 24,080, 31,430 and 24,738 data points, respectively. A small number of extreme outliers are excluded from the plots shown.

satellite pairs, although for *Wind*-ACE, the *r*-value is higher than either for DSCOVR-ACE or DSCOVR-*Wind*. The slopes of the v_y and v_z trend lines all deviate significantly from unity, but show some consistency between v_y and v_z.

In Figure 6, we display regression results for proton density and temperature as log-log plots. *Wind* versus ACE exhibit the strongest correlations ($r = 0.95$ for density and 0.93 for temperature). The trend line slopes for all three density comparisons are close to unity; this is also the case for the *Wind*-ACE temperature comparison. However, the slopes for the temperature comparisons involving DSCOVR are both above 3 due to the wide scatter of data points above $\sim 10^5$ K as measured by DSCOVR.

4.2. Monthwise Correlations

Figure 7 displays time series of DSCOVR-*Wind* *r*-values for B_z, v_x, proton density, and temperature, calculated for each month between July 2016 and December 2020. Despite some fluctuations from month to month, the monthwise correlations are typically strong for B_z, v_x, and density (following generally accepted convention, we define a strong correlation as $|r| > 0.7$, a moderate correlation as $0.5 < |r| < 0.7$, and a weak correlation as $|r| < 0.5$.) The vertical lines mark the occurrence of several software and ground processing patches designed to improve the performance of the Faraday Cup (J. Johnson, private communication).

For B_z, the correlation strength reaches its minimum ($r = 0.65$) in January 2019, which is the only month in which it falls below 0.7. For v_x, the only month in which *r* falls below 0.7 is August 2017, although additional local minima appear in April 2018 ($r = 0.78$) and December 2020 ($r = 0.79$). For density, 89% of all monthwise

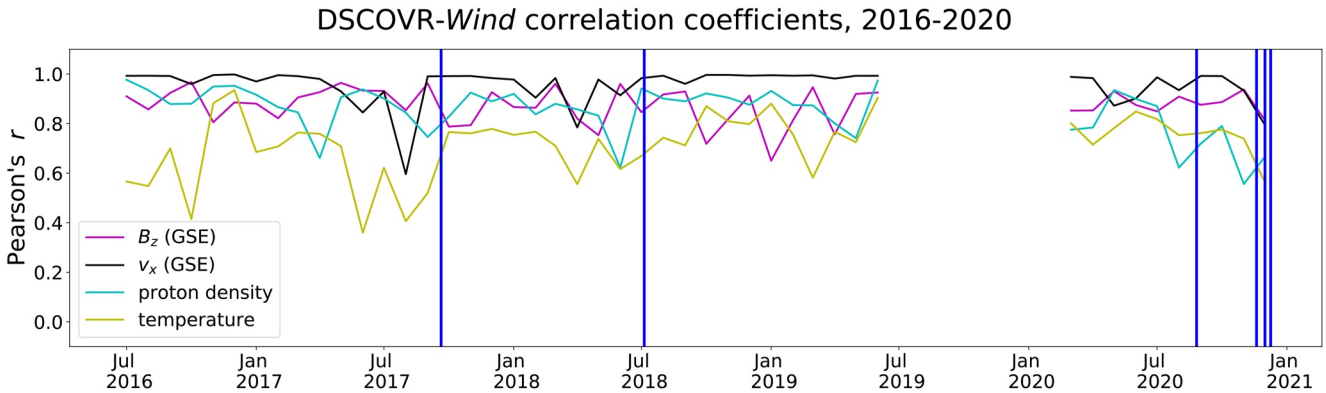

Figure 7. Time series of Deep Space Climate Observatory (DSCOVR)-*Wind r* values for B_z, v_x, proton density, and temperature, overlaid with blue lines indicating dates of Faraday Cup patches. Between July 2019 and February 2020, useable DSCOVR data were unavailable, leading to the gap visible here. A total of 46 data points for each parameter are represented in this plot.

r-values are above 0.7 with the lowest ($r = 0.56$) appearing in November 2020. The fluctuations in correlation strength are more pronounced for temperature with *r*-values ranging from 0.36 to 0.94. Although correlations for all variables shown in the figure tend to decrease at the end of the period studied; as noted above, there were other periods where correlation values dipped.

Biesecker and Johnson (2018) gave a summary of the status of the DSCOVR data and stated that the FC data did not meet requirements during periods of low solar wind density. The 2017 and 2018 patches were expected to have some success in correcting this problem. However, faulty grounding in the FC required changes to its operating mode, and those changes have caused gradual degradation over the years in the quality of the FC data at low solar wind speeds. This is confounded by less accurate background subtractions when the solar wind signal is low. Since these issues mainly occur during low solar wind speed periods, this probably explains the lack of conclusive evidence in Figure 7 of overall science data degradation over the mission. Analyzing data through 2021 and beyond would help determine if the decreased correlations observed at the end of the study period are indicative of more long-term degradation.

Quantifying the casual relationship between periods of decreased correlation in Figure 7 and all FC issues is beyond the scope of this study. However, the major cause of occasional dips in v_x correlation, observed in August 2017, April 2018, and December 2020, is well understood. For each month, significant discrepancies between DSCOVR and *Wind* v_x spanned only a few days (26–29 August 2017; 15–25 April 2018; and 1–8 December 2020) with good agreement throughout the rest of the month. Figure 8 shows DSCOVR and *Wind* v_x values, overlaid with concurrent density measurements, for a few days in August 2017 and December 2020. When the solar wind is slow, warm, or sparse, the FC can fail to resolve the peak amplitude of the solar wind signal, which leads to larger errors in v_x determination (M. Stevens, private communication). Difficulties calculating accurate background subtractions during low solar wind conditions further compound the errors. The top panels of Figure 5 also show this effect with large spreads in DSCOVR v_x during low ACE and *Wind* $|v_x|$ values.

We did attempt to establish a correlation between low densities and dips in v_x correlation for each of the three time periods. From 1–8 December 2020, the difference between the v_x measurements tends to be higher during periods of low density; we find a moderate-to-strong negative correlation ($r = -0.68$) between ambient density and v_x difference (i.e., $|v_{x,\mathrm{DSCOVR}} - v_{x,Wind}|$). This effect is not clearly observed for the other two periods of poor agreement; for 26–29 August 2017 and 15–25 April 2018, we find $r = -0.20$ and $r = -0.09$, respectively.

In Table 3, we present the results of an additional correlation analysis, which probes for covariance between monthwise DSCOVR-*Wind* *r*-values and corresponding monthly averages of spacecraft separation, solar wind speed (as measured by *Wind*), and proton density (as measured by *Wind*). By "speed," here, we mean the magnitude of the velocity, that is, $v = \sqrt{v_x^2 + v_y^2 + v_z^2}$. In most cases, these relationships are very weak ($|r| < 0.3$) or nonexistent ($|r| \approx 0$), although a moderate negative correlation ($r = -0.66$) exists between correlation strength for B_z and spacecraft separation. This indicates that the agreement between the DSCOVR and *Wind* B_z measurements tends to decrease when the satellites are farther apart. We also find a moderate positive correlation ($r = 0.51$) between the DSCOVR-*Wind* density correlation strength, which means that the DSCOVR-*Wind* density comparisons tend to agree more when *Wind* density increases.

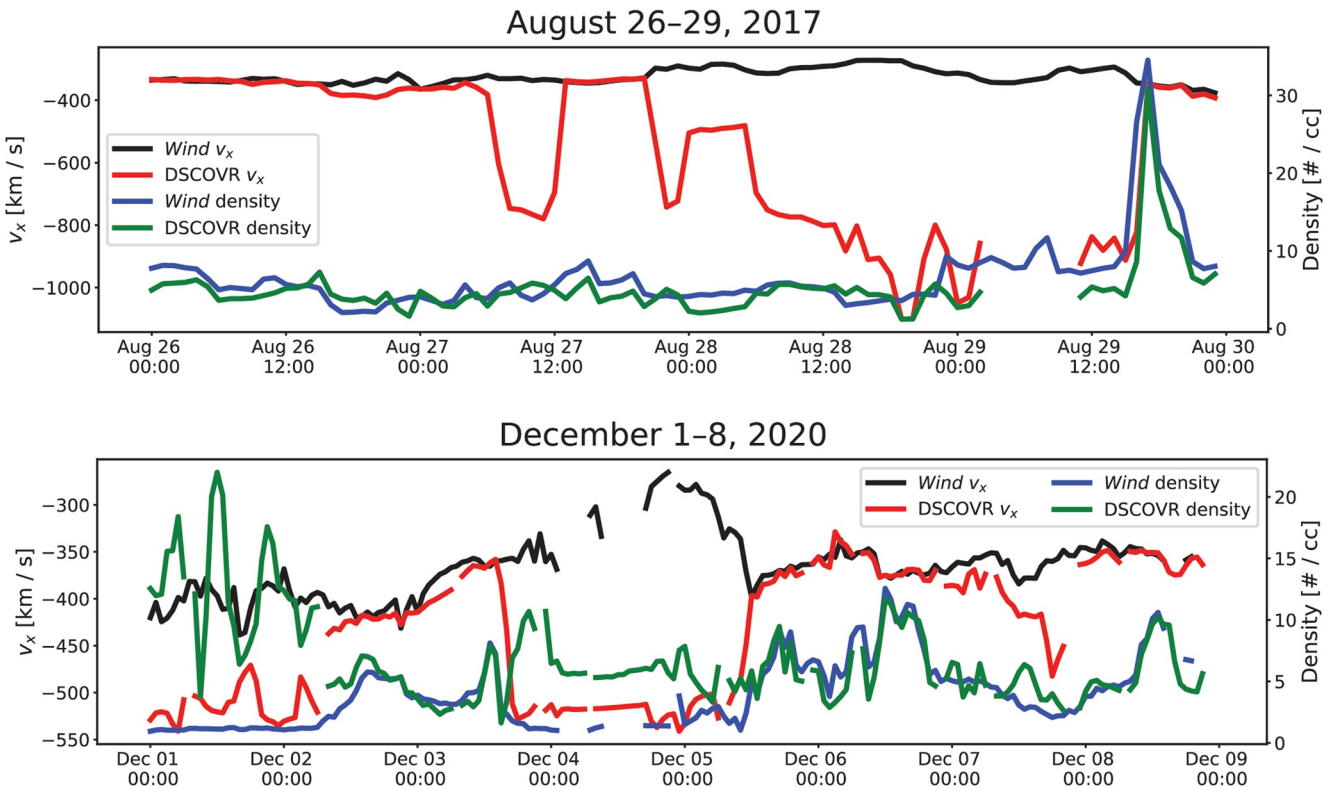

Figure 8. top: Deep Space Climate Observatory (DSCOVR) (red) and *Wind* (black) v_x values during a period in August 2017 that showed strong disagreement for v_x. *Wind* and DSCOVR density values are shown in blue and green, respectively. There is no significant correlation between *Wind* density and the absolute difference between DSCOVR and *Wind* v_x values during this 4-day period. bottom: DSCOVR (red) and *Wind* (black) v_x values during a period of particularly poor alignment in December 2020. *Wind* and DSCOVR density values are shown in blue and green, respectively. There is a moderate negative correlation ($r = -0.68$) between *Wind* density and the absolute difference between DSCOVR and *Wind* v_x values during this 8-day period.

The results in Table 3 indicating that IMF-B_z observations are sensitive to spacecraft orbit parameters at L1 were also found by King and Papitashvili (2005), who presented a statistical comparison of ACE and Wind solar wind data from NASA-CDAWeb. King and Papitashvili included the effect of spacecraft separation on their cross-satellite comparisons by implementing an impact parameter (IP), defined therein *as the distance by which a downstream spacecraft misses seeing a plasma element previously seen by an upstream spacecraft*. IP is a function of spacecraft position vector (x_i, y_i, z_i, where i is the spacecraft 1 or 2) and can be calculated from $\sqrt{\left[(y_1 - y_2) + (x_1 - x_2)/13\right]^2 + (z_1 - z_2)^2}$, assuming a radial solar wind speed of 390 km/s. They also utilized weighted regressions, in which the slope and intercept of the linear trend line are determined by minimizing a chi-square function. We incorporated King and Papitashvili's IP threshold and a weighting protocol in our DSCOVR analysis (results are not presented here) but no appreciable improvement in either trend line equations or Pearson's r values was found.

Table 3
Comparison of Deep Space Climate Observatory-Wind Correlation Strength for the Four Parameters in Figure 7 (One Data Point for Each Month From July 2016 to December 2020) Against Monthly Averages of Spacecraft Separation, Solar Wind Speed (as Measured by Wind), and Proton Density (as Measured by Wind)

	r (B_z)	r (v_x)	r (Density)	r (Temperature)
Average separation	−0.66	−0.09	0.10	0.20
Average speed (*Wind*)	0.14	0.06	0.00	−0.32
Average density (*Wind*)	−0.08	0.09	0.51	0.29

Note. The values in the table are the correlation coefficients (Pearson's r) for each time series combination.

Previous studies show that IMF parameters are better correlated over spatial scales during solar maximum compared to solar minimum (Collier et al., 1998; King & Papitashvili, 2005). Since the data period for analysis was taken from the declining phase of solar cycle 24 as the cycle moved toward minimum, this may explain the negative correlation between DSCOVR and *Wind* B_z measurements with satellite separation. The spatial scale over which plasma parameters remain relatively constant is less dependent on the solar cycle compared to IMF parameters (King & Papitashvili, 2005).

Further quantitative analyses of separation effects are beyond the scope of this study. However, in Figure 9, we display how spacecraft separation affects cross-satellite scatterplots for some solar wind parameters by coloring the

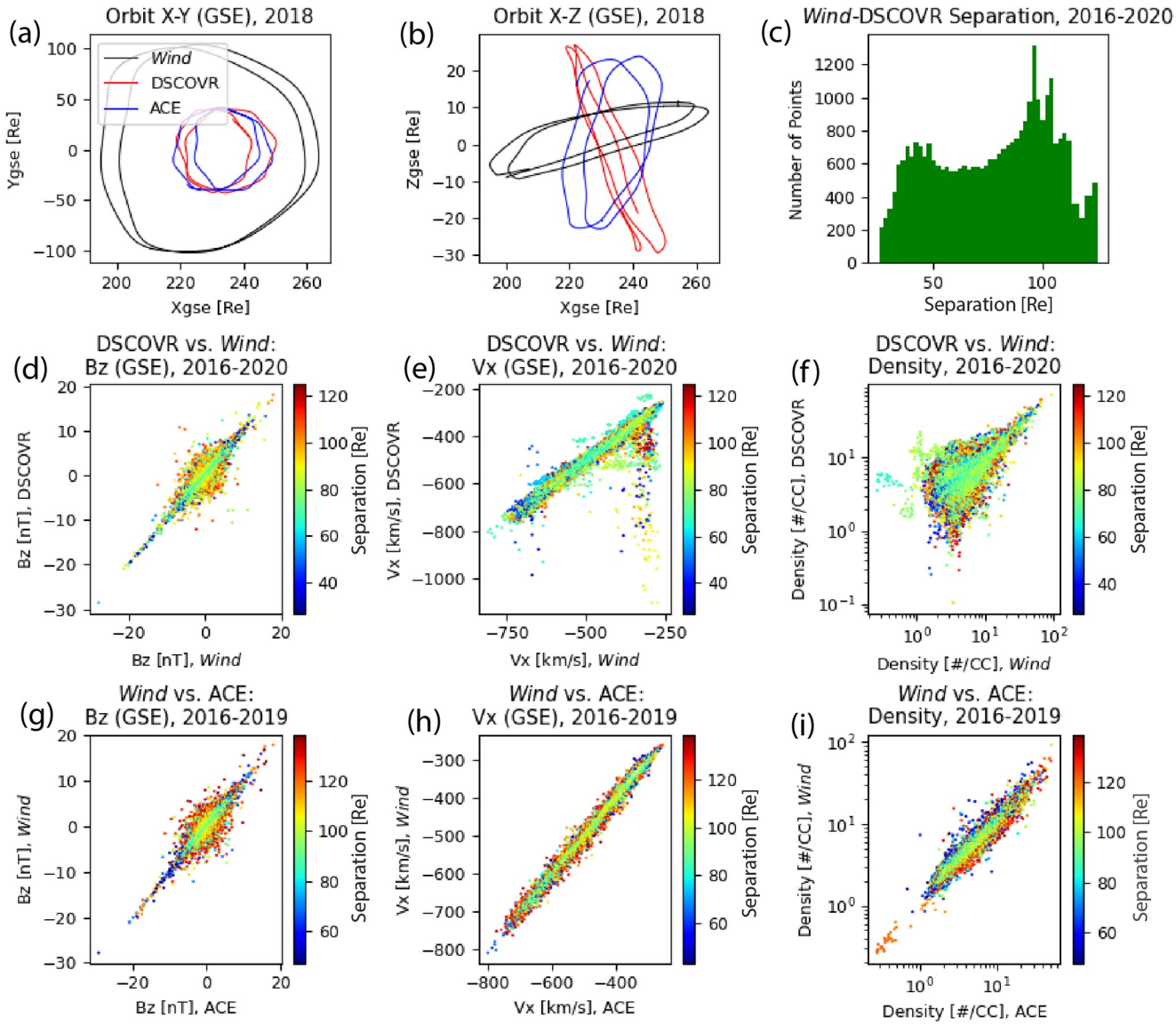

Figure 9. (a, b) Orbit trajectories of Deep Space Climate Observatory (DSCOVR), *Wind*, and Advanced Composition Explorer (ACE) during 2018. (c) Distribution of hourly averaged values of separation, in Earth radii [Re], between *Wind*-DSCOVR over data period studied (2016–2020). (d, e, f) Scatterplot of DSCOVR versus *Wind* hourly averaged B_z(GSE), v_x(GSE), and proton density, respectively, color coded by their separation in Earth radii (Re). (g, h, i): The same as panels (d, e, f) but for *Wind* versus ACE.

data points according to total separation $\left(\sqrt{x^2+y^2+z^2}\right)$. DSCOVR, *Wind*, and ACE spacecraft orbits are also shown. Panels (a) and (b) show that DSCOVR and ACE have similar L1 orbits, while the orbit of *Wind* has a significantly larger radius in the Xgse-Ygse plane. Panel c shows the distribution of hourly averaged values of separation, in Earth radii [Re], between *Wind* and DSCOVR over the time period studied. The *Wind*-ACE separation has a similar shape except peaking around 130 Re.

The B_z scatterplots (d and g) show that increasing separation results in data points being located further away from the linear curve trend. Visual inspection of the B_z scatter plots suggests that a 120 Re spacecraft separation can result in a ~5 nT difference. Interestingly, for the v_x and proton density panels (e, f, h, and g), values observed both close to minimal separations (dark blue dots) and at large separations (orange and red dots) tend to appear on the outer enveloping regions of the scatter. The trend for temperature (not shown) was somewhat similar. The colors in panel (i) suggest that the *Wind* versus ACE proton density linear trend shifts to the right as the spacecraft separation increases.

4.3. Differences Based on Ratios

In Figure 10 (top), we display plots of DSCOVR-*Wind* proton density ratios (i.e., N_{DSCOVR}/N_{Wind}) that have been classified into three bins based on solar wind speed (i.e., $v = \sqrt{v_x^2 + v_y^2 + v_z^2}$) as measured by *Wind*. Adopting the thresholds used by King and Papitashvili (2005), we distinguish between slow (<350 km/s), moderate (350−450 km/s), and fast (>450 km/s) solar wind. For $v < 350$ km/s, we find the mean value of N_{DSCOVR}/N_{Wind} to be 0.78 ± 0.27. At moderate speeds, it rises to 1.07 ± 0.73, and for $v > 450$ km/s, it becomes 1.8 ± 1.06. If we restrict our focus to ratios of less than 4.0, we find means of 0.78 ± 0.21 for $v < 350$ km/s, 1.03 ± 0.35 for v between 350 and 450 km/s, and 1.69 ± 0.59 for $v > 450$ km/s. This narrower scope, selected to exclude extreme outliers, comprises 99.9% of the "slow" category, 99.5% of the "moderate" category, 97.5% of the "fast" category, and 99.0% of DSCOVR-*Wind* density ratios as a whole. Our results suggest that DSCOVR tends to underestimate the proton density when the solar wind speed is low and overestimates it when the solar wind speed is high, while DSCOVR and *Wind* provide comparable density measurements when the solar wind speed is moderate. Normalized Probability density functions for each speed bin are displayed in Figure 10 (bottom).

A simila(though weaker) trend is observed among DSCOVR-*Wind* temperature ratios (plot not shown here). For ratios less than 4.0, we find for low solar wind speeds a mean T_{DSCOVR}/T_{Wind} value of 0.86 ± 0.44; for moderate speeds 1.51 ± 0.87; and for high speeds 2.02 ± 0.86. In this case, this accounts for 92.9% of the "slow" bin, 90.9% of the "moderate" bin, 87.6% of the "fast" bin, and 90.5% of T_{DSCOVR}/T_{Wind} values overall. Results obtained using the full set can be found in Table 4.

When we sort the DSCOVR-*Wind* v_x ratios by *Wind* speed, we find means close to unity with a minimal spread for each bin. However, no dependencies were found for v_y and v_z ratios. Likewise, we found no clear speed dependence among B_z ratios. We note that the spreads in $B_{z,DSCOVR}/B_{z,Wind}$ are fairly large, and so the averages we report should not be taken as conclusive evidence of a tendency for DSCOVR to underestimate B_z measurements. See Table 4 for details.

We repeat this analysis for proton density, sorting DSCOVR-*Wind* ratios into low- and high-density bins (≤5/cc and >5/cc, respectively) based on the *Wind* measurements. At low densities, $N_{DSCOVR}/N_{Wind} = 1.62 \pm 1.19$ on average, compared with 0.92 ± 0.27 at high densities (see Figure 10). If we implement the 4.0 ratio threshold, the mean N_{DSCOVR}/N_{Wind} value falls to 1.49 ± 0.66 for low density; the high-density value is unchanged. Density ratios of less than 4.0 comprise 97.6% of the "low-density" bin and 100% of the "high-density" bin. Shifting our focus to temperature and limiting T_{DSCOVR}/T_{Wind} to less than 4.0, we find means of 1.97 ± 0.98 for $N_{Wind} \leq 5$/cc (representing 83.2% of the "low-density" bin), compared to 1.17 ± 0.65 for $N_{Wind} > 5$/cc (representing 95.4% of the "high-density" bin). This suggests that DSCOVR tends to overestimate both density and temperature when the ambient proton density is low, while its measurements of these parameters are more likely to agree with *Wind* at higher densities.

We observe, as we would again expect, that DSCOVR and *Wind* v_x values are comparable across density bins. Moreover, there is no discernible density dependence in either v_y, v_z, or B_z. As before, the large spreads in $B_{z,DSCOVR}/B_{z,Wind}$ values limit the utility of this particular finding. The results are summarized in Table 5.

5. Discussions and Conclusions

In this study, we validated DSCOVR MAG and FC data against equivalent *Wind* and ACE science data. DSCOVR magnetic field observations show good statistical agreement with *Wind* and ACE measurements over the period studied. IMF-B_z showed the lowest correlation for all three satellite comparisons (see bottom panel of Figure 4). Signs of significant degradation over time using monthly values were inconclusive between DSCOVR-*Wind* B_z, although this monthwise analysis was not repeated for *Wind*-ACE.

The results for the DSCOVR FC solar wind particle comparisons to *Wind* and ACE are more mixed. The v_y and v_z components of the solar wind can influence space weather, for example, the orientation of the geomagnetic tail and consequently the regions of space, and tail processes, that surround satellites in that region. However, the solar wind bulk speed is dominated by the v_x-component as seen in Figure 5. In other words, the solar wind is mainly radial. Hence, the resulting lower correlation for v_y and v_z is less consequential on space weather forecasting capabilities.

For individual days, there are times where DSCOVR v_x measurements deviated significantly from *Wind* (see Figure 8). This tends to happen when *Wind* v_x measurements are low as shown in the top panels of Figure 5. The

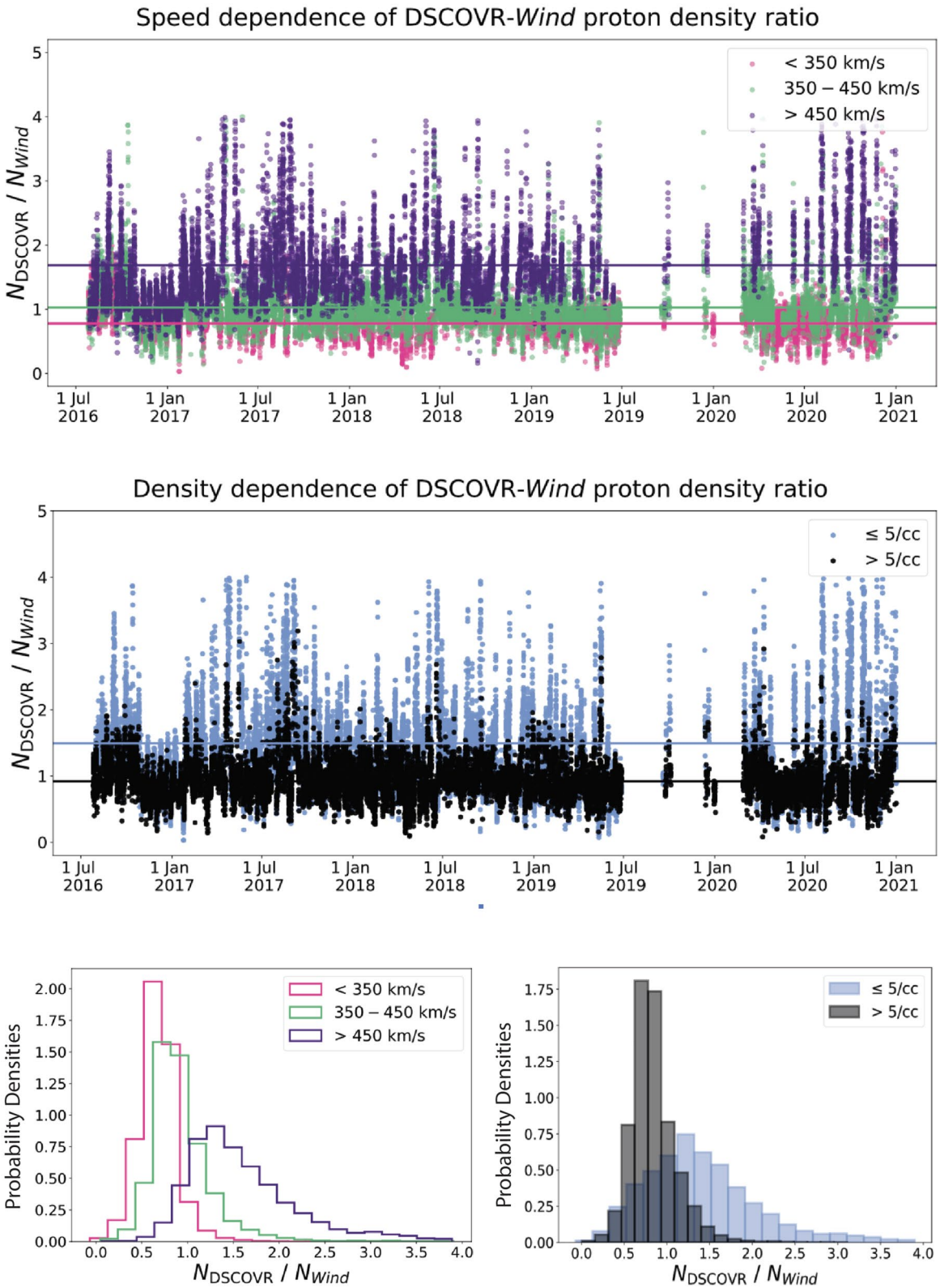
Speed dependence of DSCOVR-Wind proton density ratio
< 350 km/s
350 – 450 km/s
> 450 km/s
N_DSCOVR / N_Wind
1 Jul 2016
1 Jan 2017
1 Jul 2017
1 Jan 2018
1 Jul 2018
1 Jan 2019
1 Jul 2019
1 Jan 2020
1 Jul 2020
1 Jan 2021
Density dependence of DSCOVR-Wind proton density ratio
≤ 5/cc
> 5/cc
N_DSCOVR / N_Wind
Probability Densities
N_DSCOVR / N_Wind

Figure 10.

Table 4
Means and Standard Deviations of DSCOVR-Wind Ratios for Proton Density, Temperature, Solar Wind v_x (GSE), and B_z (GSE), Classified Into Three Bins Based on Solar Wind Speed (as Measured by Wind)

	N_{DSCOVR}/N_{Wind}	T_{DSCOVR}/T_{Wind}	$v_{x,DSCOVR}/v_{x,Wind}$	$B_{z,DSCOVR}/B_{z,Wind}$
<350 km/s	0.78 ± 0.27	1.69 ± 4.54	1.02 ± 0.16	0.91 ± 19.61
	0.78 ± 0.21	*0.86 ± 0.44*	*1.02 ± 0.16*	*0.79 ± 0.99*
350–450 km/s	1.07 ± 0.73	1.99 ± 2.1	1.02 ± 0.04	0.63 ± 40.15
	1.03 ± 0.35	*1.51 ± 0.87*	*1.02 ± 0.04*	*0.79 ± 1.02*
>450 km/s	1.8 ± 1.06	2.48 ± 1.66	1.01 ± 0.03	0.7 ± 80.7
	1.69 ± 0.59	*2.02 ± 0.86*	*1.01 ± 0.03*	*0.74 ± 1.08*

Note. Ratios are computed from hourly averages spanning the full range of this analysis (2016–2020). Italicized values are the results when we limit our focus to ratios of magnitude less than 4.0. DSCOVR, Deep Space Climate Observatory; GSE, Geocentric Solar Ecliptic.

root cause is electrical grounding issues with the FC, which results in difficulty resolving solar wind peak amplitudes and inaccuracies in background subtractions during low solar wind conditions. However, the color coding in the upper panels in Figure 5 indicates that even at low solar wind conditions, as measured by *Wind* and ACE, a significant portion of data points still fall close to the v_x linear trend lines when compared to DSCOVR.

Our analysis of density ratios also indicates that statistically there is a dependency of solar wind speed (slow, medium, or fast) on whether DSCOVR density estimates are below *Wind*, about equal to *Wind*, or higher than *Wind* density measurements. The medium solar wind speed (350–450 km/s) seems to be a sweet spot where DSCOVR and *Wind* density estimates are about equal, while DSCOVR density observations tend to overestimate compared to *Wind* when solar wind densities are low (below ∼5 cc).

Cross-satellite comparisons can be affected by spacecraft separation. The correlation between DSCOVR and *Wind* B_z values was found to decrease with increasing spacecraft separation. Monthly averages were used to determine the correlation value in Table 3 because *Wind* takes more than 6 months to complete a halo orbit at L1. Qualitatively, the separation effect on cross-satellite B_z comparisons can also be seen in Figures 9d and 9g where hourly averaged B_z values are colored according to spacecraft separation.

It is unclear why cross-satellite comparisons of v_x and proton density at minimal separations and at large separations tend to appear on the outer enveloping regions of the scatter plots (see Figures 9e–9i). One possibility is a dependency on the separation direction. We undertook an initial analysis of separation effects along the Xgse, Ygse, and Zgse directions, but results (not shown) did not indicate any significant differences compared to the analysis using only total separation distances. Studying the spatial scales along different axes under different solar wind flow types (e.g., corotating interacting regions and coronal mass ejections) would be useful but beyond the scope of this study. However, given the importance of solar wind parameters (particularly the IMF) in space weather prediction and forecasting, we recommend more studies be undertaken to better inform the dependency of L1 observations on spacecraft separation and spatial scales.

Cross-satellite validation of particle measurements taken in space is challenging. Particle detectors are complex instruments relying on count statistics and cross-satellite comparisons of these detectors are complicated by many factors, including differences in detector responses across instruments, design differences, degradation, and other factors. However, overall, the DSCOVR density calculations showed good agreement with *Wind* and ACE and also better correlations than for temperature. The temperature being a second-order moment statistically amplifies errors associated with lower-order estimates, such as density. Therefore, it is not surprising that correlations were lowest for temperature.

Faraday Cups are tuned to velocity distributions, and with v_x dominating the solar wind speed, we also expected that v_x would show the best correlation. However, the moment estimates assume that the proton velocity distribution function (VDF) is isotropic because the algorithm uses a 1D VDF. There are often anisotropic conditions, which make this assumption less valid.

Taking all results into consideration, we are able to make concluding statements about the accuracy of the DSCOVR hourly averaged major solar wind parameters (B_z, v_x, proton density, and proton temperature) data. Table 6 shows accuracy estimates assuming *Wind* data is truth, and restricting data to regions where the DSCOVR-*Wind* separation is ≤80 R_e. The amount of hourly data used for each accuracy estimate is also shown.

The root-mean-square error (RMSE) for B_z is < ±1.0 nT without restricting solar wind speed. The B_z ratio standard deviations shown in Table 4 are somewhat misleading because B_z measured at L1, averaged over many

Figure 10. top: Time series of Deep Space Climate Observatory (DSCOVR)-*Wind* proton density ratios categorized by solar wind speed as measured by *Wind*. Ratios are computed from hourly averages spanning the full range of this analysis (2016–2020). Mean values are indicated by horizontal lines. bottom: Normalized probability density functions (PDFs) for each category (n_{bins} = 20 in each case). The "slow" PDF (<350 km/s) represents 8,998 data points; the "moderate" PDF (350–450 km/s) represents 13,012 data points; and the "fast" PDF (>450 km/s) represents 9,116 data points. For the ratios categorized by *Wind* density, ≤5/cc represents 12,399 data points and >5/cc represents 18,727 data points. In each of the plots above, we limit our consideration to ratios of less than 4.0.

Table 5
Means and Standard Deviations of DSCOVR-Wind Ratios for Proton Density, Temperature, Solar Wind v_x (GSE), and B_z (GSE), Classified Into Two Bins Based on Proton Density (as Measured by Wind)

	N_{DSCOVR}/N_{Wind}	T_{DSCOVR}/T_{Wind}	$v_{x,DSCOVR}/v_{x,Wind}$	$B_{z,DSCOVR}/B_{z,Wind}$
≤5/cc	1.62 ± 1.19	2.79 ± 3.36	1.02 ± 0.11	1.03 ± 60.29
	1.49 ± 0.66	*1.97 ± 0.98*	*1.02 ± 0.1*	*0.73 ± 1.09*
>5/cc	0.92 ± 0.27	1.55 ± 2.5	1.01 ± 0.08	0.53 ± 45.68
	0.92 ± 0.27	*1.17 ± 0.65*	*1.01 ± 0.08*	*0.8 ± 0.98*

Note. Ratios are computed from hourly averages spanning the full range of this analysis (2016–2020). Italicized values are the results when we limit our focus to ratios of magnitude less than 4.0. DSCOVR, Deep Space Climate Observatory; GSE, Geocentric Solar Ecliptic.

Table 6
Accuracy of Deep Space Climate Observatory Hourly Averaged In-Situ Observations Assuming Wind Is Truth

Parameter[a]	Amount of data[b]	Accuracy
B_z	~21 months	<±1.0 nT (RMSE)
v_x (<350 km/s)	~6 months	12% (1σ)
v_x (≥350 km/s)	~15 months	4% (1σ)
Proton density (≤5/cc)	~8 months	65% (1σ)
Proton density (>5/cc)	~12 months	27% (1σ)
Proton temperature (≤5/cc)	~6 months	98% (1σ)
Proton temperature (>5/cc)	~12 months	66% (1σ)

[a]The limits are based on *Wind* observations. [b]Data are restricted to DSCOVR-*Wind* separations of ≤80 R_e and only ratios of magnitude less than 4.0 are considered.

years, is ~0 nT and the ratio of two numbers close to zero can be large just by statistical chance. Hence, the B_z ratios were not used to determine accuracy.

For solar wind plasma parameter accuracy, the standard deviation (1σ) of the DSCOVR-*Wind* ratio is subtracted from a ratio of 1.0 and converted to a percentage. The ratio values used are also restricted to <4.0. We decided to split the v_x accuracy in Table 6 into two groups, v_x accuracy when the solar wind speed as measured by *Wind* is <350 km/s and ≥350 km/s. This was because the results in Table 4 show similar standard deviations between the medium and high solar wind speed cases for v_x. The mean of the v_x ratio is ~1.0 and therefore using the standard deviation only is justified. For the proton density and temperature results, we show results for the two density cases ≤5/cc and >5/cc. When adding ±1σ to the means, both density and temperature ratios include 1.0 and therefore we only report the 1σ values in Table 6. Note, the accuracy values shown in the table would not change significantly if we had estimated the percentages using the RMSE between the observed ratios and a predicted ratio of 1.0.

In general, the values shown in Table 6 for v_x, proton density, and temperature are similar to that shown in Table 4 for ratio cases restricted to <4.0. Hence, restricting the data used to DSCOVR-*Wind* separations ≤80 R_e makes little difference to the statistical results. We also calculated values in the table using different separation ranges while maintaining about the same amount of data in each separation bin so as to not bias outcomes, but the results were not significantly different.

The DSCOVR data used in this study are the NCEI archive of real-time NOAA DSCOVR space weather operational data. This data set has not been reprocessed, like ACE and *Wind* data, to improve data quality and science quality. Furthermore, the DSCOVR data presented are hourly averages of the high-resolution operational archive. Caution is advised when drawing conclusions based on these results about the high-resolution data set.

For operations, a simple robust moment method (Stevens et al., 2014) was employed for DSCOVR solar wind parameter estimations. However, reprocessed 1-min resolution FC data set using a nonlinear fitting method and covering time periods in 2016–2019 is available on the NASA-CDAWeb. The DSCOVR space weather data, particularly with ACE aging well beyond its operational mission lifetime, provides an important contribution to both NOAA's space weather operations and space weather research in the science community.

Data Availability Statement

Space weather data from NOAA's DSCOVR spacecraft, archived with identifiers at the NOAA-NCEI (NOAA, 2016), were used in the creation of this manuscript. Also used in this creation of this manuscript were magnetic field and particle data from the *Wind* spacecraft, which are archived and have identifiers as described by Koval et al. (2021) and Lazarus et al. (2021), respectively. Access to the ACE magnetic field and particle data used in the creation of this manuscript is described by Smith and Ness (2022) and McComas et al. (2022), respectively. Data analyses were accomplished using the Python programming language (https://www.python.org) and figures were also created using Python. All Python releases are Open Source (see https://opensource.org/ for the Open Source Definition).

Acknowledgments
This work was supported by the NOAA Cooperative Agreement with CIRES-University of Colorado, NA17OAR4320101. The views, opinions, and findings contained in this report are those of the authors and should not be construed as an official National Oceanic and Atmospheric Administration, National Aeronautics and Space Administration, or other U.S. Government position, policy, or decision.

References

Belcher, J. W. (1973). A variation of the Davis-Smith method for in-flight determination of spacecraft magnetic fields. *Journal of Geophysical Research*, *78*(28), 6480–6490. https://doi.org/10.1029/JA078i028p06480

Belcher, J. W., Davis, L., Jr., & Smith, E. J. (1969). Large-amplitude Alfvén waves in the interplanetary medium: Mariner 5. *Journal of Geophysical Research*, *74*(9), 2302–2308. https://doi.org/10.1029/JA074i009p02302

Biesecker, D., & Johnson, J. (2018). DSCOVR—Status update and comparing data from l1. In *The space weather workshop*.
Boggs, P. T., Spiegelman, C. H., Donaldson, J. R., & Schnabel, R. B. (1988). A computational examination of orthogonal distance regression. *Journal of Econometrics*, *38*(1), 169–201. https://doi.org/10.1016/0304-4076(88)90032-2
Collier, M. R., Slavin, J. A., Lepping, R. P., Szabo, A., & Ogilvie, K. (1998). Timing accuracy for the simple planar propagation of magnetic field structures in the solar wind. *Geophysical Research Letters*, *25*(14), 2509–2512. https://doi.org/10.1029/98GL00735
Connerney, J. E. P. (2013). *(DSCOVR) project magnetometer calibration plan DSCOVR-MAG-cal-0001 revision (3)* (Tech. Rep.). NASA Goddard Space Flight Center.
Davis, L. J., & Smith, E. J. (1968). The in-flight determination of spacecraft magnetic field zeros. *Eos, Transactions American Geophysical Union*, *49*(257), 1563–1569.
Kasper, J., Case, A., & Szabo, A. (2013). *Design and early observations from the dscovr solar wind faraday cup* (Tech. Rep.). NASA Goddard Space Flight Center.
King, J. H., & Papitashvili, N. E. (2005). Solar wind spatial scales in and comparisons of hourly wind and ace plasma and magnetic field data. *Journal of Geophysical Research*, *110*(A2), A02104. https://doi.org/10.1029/2004ja010649
Koval, A., Lepping, R. P., & Szabo, A. (2021). Wind magnetic field investigation (MFI) composite data [Dataset]. NASA Space Physics Data Facility. https://doi.org/10.48322/av38-wn55
Lazarus, A. J., Candey, R. M., Kasper, J. C., Ogilvie, K. W., & Fitzenreiter, R. J. (2021). Wind solar wind experiment (SWE) thermal plamsa moments, key parameter (k0), 99 s data [Dataset]. NASA Space Physics Data Facility and the Massachusetts Institute of Technology. https://doi.org/10.48322/3zky-gy15
McComas, D., Skoug, R., Delapp, D., Elliott, H., & Davis, A. (2022). ACE solar wind electron, proton, and alpha monitor (SWEPAM) plasma moments, level 2 (H2), 1 h data [Dataset]. NASA Space Physics Data Facility. https://doi.org/10.48322/9w01-2555
NOAA. (2016). NOAA space weather prediction center: Deep space climate observatory (DSCOVR) [Dataset]. NOAA National Centers for Environmental Information. https://doi.org/10.7289/V51Z42F73
Ogilvie, K. W., Chornay, D. J., Fritzenreiter, R. J., Hunsaker, F., Keller, J., Lobell, J., et al. (1995). SWE, a comprehensive plasma instrument for the wind spacecraft. *Space Science Reviews*, *71*(1), 55–77. https://doi.org/10.1007/BF00751326
Smith, C. W., & Ness, N. (2022). ACE magnetic field (MAG) geocentric solar ecliptic, GSE, and geocentric solar magnetospheric, GSM, coordinates, level 2 (H2), 1 h data [Dataset]. NASA Space Physics Data Facility. https://doi.org/10.48322/fh85-fj47
Stevens, M. L., Kasper, J. C., Case, A., & Koval, A. (2014). *DSCOVR faraday cup level 1b theoretical basis document* (Tech. Rep.). NASA Goddard Space Flight Center.
Szabo, A. (2014). Deep space climate observatory (DSCOVR). In *The 6th NASA space weather and robotic mission operations workshop*.
Szabo, A. (2015). Dscovr instrumentation capabilities and calibration test plan. In *The space weather workshop*.
Szabo, A., & Koval, A. (2016). Dscovr magnetometer observations. In *The space weather workshop*.